

Article

Cyclic Ablation Properties of C/SiC-ZrC Composites

Hailang Ge^{1,2}, Lu Zhang^{1,*} , Huajun Zhang³, Fang Wang⁴, Xiguang Gao¹ and Yingdong Song^{1,5}

¹ College of Energy and Power Engineering, Nanjing University of Aeronautics and Astronautics, Nanjing 210016, China

² College of Mechanical and Electrical Engineering, Suqian University, Suqian 223800, China

³ Second Military Representative Office of the Chinese People's Liberation Army, Chengdu 610000, China

⁴ College of Chemical Engineering, Nanjing Forestry University, Nanjing 210037, China

⁵ Harbin Engineering University, Harbin 150006, China

* Correspondence: luzhang@nuaa.edu.cn

Abstract: To reveal the ablation performance of C/SiC-ZrC composites under different ablation modes, C/SiC-ZrC composites were prepared using chemical vapor deposition, precursor infiltration, and pyrolysis. Single ablation and cyclic ablation tests were conducted on the C/SiC-ZrC composites using an oxyacetylene flame, in order to obtain ablation parameters, as well as macroscopic and microscopic ablation morphology for the different ablation modes. The results show that the linear ablation rate and mass ablation rate of different ablation modes decrease with increasing time. The linear ablation rate and mass ablation rate of cyclic ablation are 12% and 24.2% lower than those of single ablation. Within the same ablation time, the C/SiC-ZrC composites subjected to cyclic ablation exhibit shallower and more evenly distributed pits, caused by high-temperature airflow ablation. The material surface has a white oxide layer composed of SiO₂ and ZrO₂, and the carbon fibers inside are wrapped by oxide particles, enhancing the ablation resistance of C/SiC-ZrC composites.

Keywords: C/SiC-ZrC composites; cyclic ablation; microscopic structure; ablation mechanism



Citation: Ge, H.; Zhang, L.; Zhang, H.; Wang, F.; Gao, X.; Song, Y. Cyclic Ablation Properties of C/SiC-ZrC Composites. *Aerospace* **2024**, *11*, 432. <https://doi.org/10.3390/aerospace11060432>

Academic Editors: Yosheph Yang and Ikhyun Kim

Received: 19 April 2024

Revised: 22 May 2024

Accepted: 23 May 2024

Published: 27 May 2024



Copyright: © 2024 by the authors. Licensee MDPI, Basel, Switzerland. This article is an open access article distributed under the terms and conditions of the Creative Commons Attribution (CC BY) license (<https://creativecommons.org/licenses/by/4.0/>).

1. Introduction

With the continuous development of the Rotating Detonation Engine (RDE), the demand for high-temperature resistance, especially ablation resistance, of combustion chambers and nozzles is also increasing [1–4]. Ceramic matrix composites (CMCs) are widely regarded as the most promising thermal protection materials due to their excellent high-temperature resistance, oxidation resistance, and ablation resistance [5,6]. However, CMCs may undergo thermal ablation and damage structural integrity in high-temperature applications [7]. Exploring the ablation mechanism of CMCs at high temperatures is of great research significance for improving the lifespan and performance of the RDE.

Many scholars have researched the ablation mechanism of composites such as C/C, C/SiC, SiC/SiC, and other composites [8–14]. CMCs have good anti-ablation performance below 2000 °C, but as the temperature continues to rise, CMCs are unable to meet the required ablation performance [15]. Many scholars have studied the ablation performance of CMCs with added refractory metal compounds. Wang [16] conducted ablation experiments on C/C-ZrC-SiC composites using plasma flames and found that ZrC and SiC were oxidized to form ZrO₂-SiO₂ binary eutectic systems, respectively. Li [17] studied the effect of different ceramic contents on the microstructure and ablation performance of materials. C/C-ZrC-SiC composites showed better ablation resistance when the ZrC and SiC contents were 27.2% and 7.56%, respectively. Tian Wei [18] doped a high-temperature ceramic matrix into C/C-SiC composites and found that during the ablation process, the surface of the composites oxidized, forming a composite layer, which hindered the transfer of oxygen and heat from the surface to the interior of the material. Liu [19] studied the ablation performance and mechanism of Cf/SiC-ZrC composites under different laser

ablation times (5 s, 10 s, and 15 s) and found that the dense structure and continuous layer with high-temperature resistance components are key factors in improving the material's ablation resistance. Xiang [20] studied the ablation oxidation behavior of C/SiC materials with different coatings and found that ZrB₂-SiC/SiC coatings can provide more effective protection for C/SiC materials. The above studies investigated the ablation performance and mechanism of composites. In other research related to ablation, such as components, ablation methods, strength, etc., Zhao [21] prepared C/C-ZrC-SiC-ZrB₂ and C/C-ZrC-SiC composite wedge-shaped components. Compared with C/C composites, these two composite components exhibited better ablation resistance. Fan [22] prepared C/SiC-Si composites with different prefabricated components. It was found that the tensile strength of 2D C/SiC-Si was higher than that of 3DN C/SiC-Si, but the mass ablation rate of 3DN C/SiC-Si was lower than that of 2D C/SiC-Si. Zhao [23] investigated the ablation test of C/C-ZrC-SiC-ZrB₂ composites using an oxygen-acetylene torch and found that the surface temperature of the C/C-ZrC-SiC-ZrB₂ composites during a cyclic ablation of 60 s × 2 was higher than that of 30 s × 4.

C/SiC composites overcome the brittleness of ceramics and have excellent oxidation resistance and ablation resistance [24–26]. There have been many studies on the mechanism of single ablation of C/SiC composites, but many high-temperature environments are not continuous. For example, the high-temperature environment of RDE is periodic [27–29]. Therefore, studying cyclic ablation can better reveal the ablation performance of materials under this working condition. The authors investigated the differences in ablation properties of 2D C/SiC and C/SiC-ZrC composites [30]. The ablation rate of C/SiC-ZrC was generally lower than that of C/SiC. This article presents a macroscopic and microscopic analysis of C/SiC-ZrC composites under single and cyclic ablation modes, comparing the effects of different ablation modes on the ablation rate and reveals the ablation performance of C/SiC-ZrC composites under different ablation modes.

2. Experimental Materials and Methods

2.1. Experimental Materials

C/SiC-ZrC ablation samples were prepared by the Institute of Metals, Chinese Academy of Sciences, using the chemical vapor deposition and precursor immersion and pyrolysis (CVD + PIP) process. As shown in Figure 1, a needle punching tool is used to hook the fiber cloth onto the lower layer to form a 2D needle-punched structural material. Then, a layer of pyrolytic carbon (PyC) interface layer is deposited on the surface of the carbon fiber, and the densification of the material matrix is completed through the CVD + PIP composite process. The parameters of the C/SiC-ZrC composites are shown in Table 1.

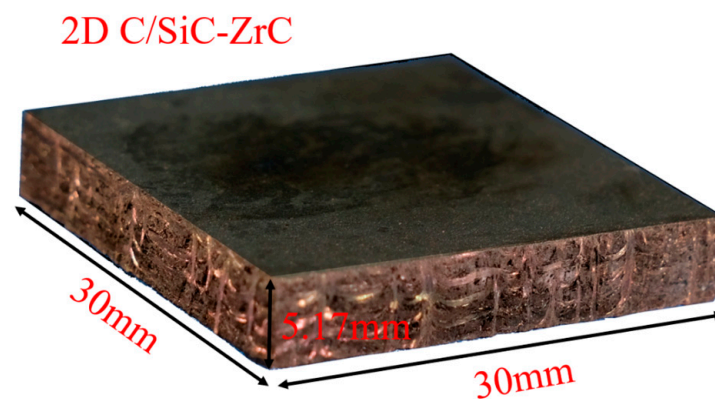


Figure 1. Two-dimensional needled C/SiC-ZrC composites.

Table 1. Parameters of materials.

C/SiC-ZrC	Value
Density (g/cm ³)	1.95
Fiber density (g/cm ³) [31]	1.8
Fiber diameter (D/μm)	5
CTE of SiC matrix: α_m [32]	4.6×10^{-6}
CTE of ZrC matrix: α_m	6.7×10^{-6}
CTE of C fiber: α_f [33]	1.12×10^{-6}

2.2. Experimental Methods

The ablation test and the testing method are carried out in accordance with the national military standard (GJB323A-96) [34]. The entire specimen is ablated using an oxygen-acetylene flame, and the ablation platform is shown in Figure 2. The ablation platform comprises an oxygen-acetylene flame nozzle, a specimen clamping device, an oxygen-acetylene gas source device, and an ablation control console. The ablation device can achieve automatic ignition, loading and unloading, and adjust the flow and pressure of oxygen and acetylene. The distance between the flame nozzle and the surface of the sample is 10 mm. The ablation ignition test is shown in Figure 2b, with a flame width of approximately 4–5 mm and a maximum flame temperature of approximately 3000 °C [35]. The sample is fixed to the rear of the sample clamping device shown in Figure 2c, and the diameter of the circular area of the sample exposed to the gas environment is $\Phi 25$ mm. The parameters of the ablation test are shown in Table 2.

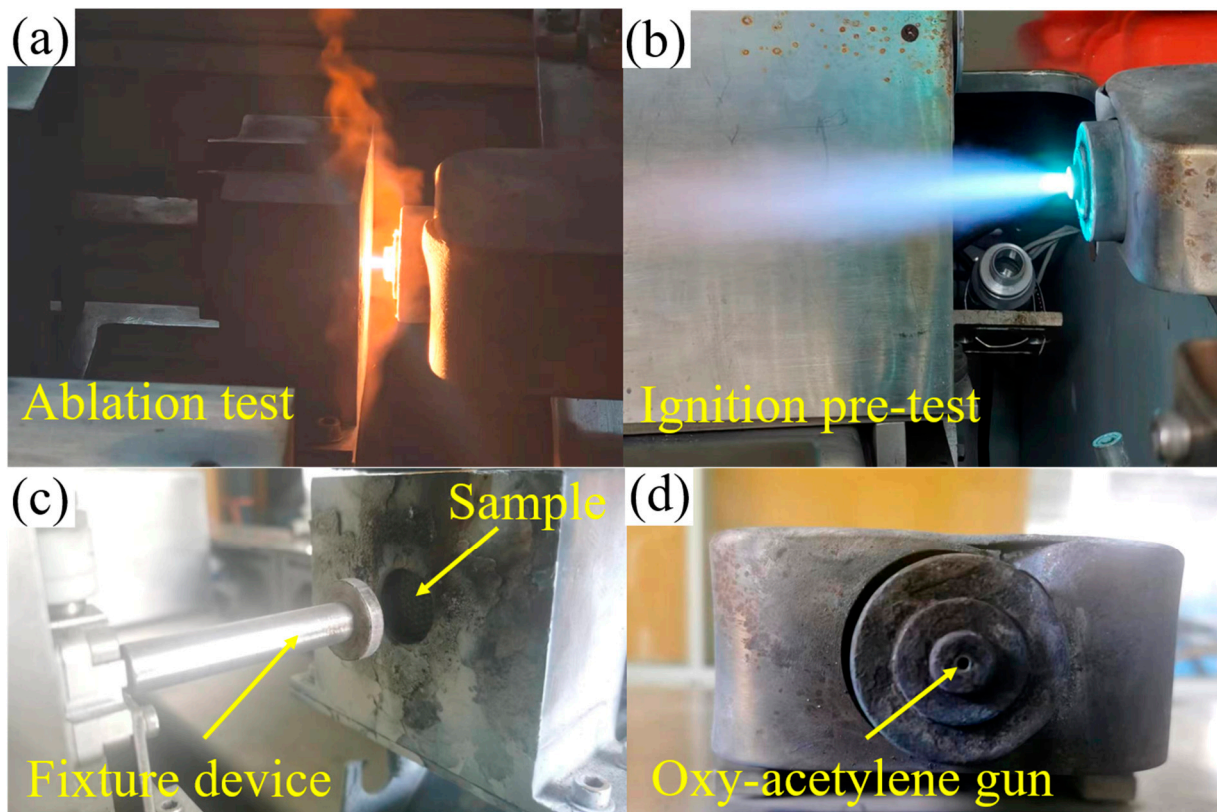


Figure 2. Ablation platform. (a) Ablation test; (b) oxy-acetylene ignition pre-test; (c) sample fixture device; (d) oxy-acetylene flame gun.

Table 2. Ablation test parameters.

O ₂ Flux (m ³ /min)	O ₂ Pressure (MPa)	C ₂ H ₂ Flux (m ³ /min)	C ₂ H ₂ Pressure (MPa)	Q (kW/m ²)	T _{max} (°C)
0.0252	0.4	0.0186	0.095	4200	3000

Using a depth gauge and an electronic scale, the initial thickness and mass of the ablated specimen are measured. Due to the uneven temperature distribution of the oxygen-acetylene flame and the uneven surface temperature of the specimen, there is a certain thermal gradient from the center of the flame to the edge of the specimen. Therefore, the thickness of three points in the ablated center area of the specimen is measured, and the average value of these measurements is used to calculate the linear ablation rate (LAR) and mass ablation rate (MAR) of the ablated specimen. The definitions of the linear ablation rate (LAR) and mass ablation rate (MAR) are as follows:

$$\text{LAR} = \frac{l_0 - l_t}{t} \quad (1)$$

$$\text{MAR} = \frac{m_0 - m_t}{t} \quad (2)$$

In the formula, l_0 and l_t represent the center thickness of the sample before and after ablation, respectively, while m_0 and m_t represent the mass of the sample before and after ablation, respectively; t is the ablation time.

The C/SiC-ZrC composites are divided into three groups for ablation testing, with two specimens in each group. The two specimens in each group undergo two types of ablation modes: single ablation and cyclic ablation. Single ablation involves ablating the specimens for 30 s, 40 s, and 60 s, respectively, whereas cyclic ablation involves ablating them for 15 s, 20 s, and 30 s, respectively. After scanning with SEM electron microscopy, the specimens undergo further ablation for 15 s, 20 s, and 30 s. The samples after a single ablation are named CSZ-30, CSZ-40, and CSZ-60, respectively, and the samples after the first cyclic ablation are named CSZ-15×1, CSZ-20×1, CSZ-30×1. Following the second ablation, they are named CSZ-15×2, CSZ-20×2, CSZ-30×2. The ablation rate at the same time is basically the same, with less variation, so the samples used to measure the ablation parameters are one instead of three. The field emission electron scanning microscope (Tescan, Czech) used is equipped with high-resolution dual beam electron microscopy (FIB-SEM), a time-of-flight secondary ion mass spectrometer (TOF-SIMS), and an energy dispersive spectrometer. This equipment allows for the micro-morphology scanning and local component analysis of the ablated sample. The macroscopic morphology of the ablated sample is reconstructed using a Reeye 3M blue light fixed industrial scanner.

3. Results and Analysis

To reveal the ablation mechanism of C/SiC-ZrC composites, the ablated samples were first scanned in three dimensions to reconstruct their macroscopic morphology after ablation. The effects of different ablation modes on the ablated samples were then compared. Subsequently, the thickness and mass changes of the sample before and after ablation were measured, and the ablation properties of the sample were analyzed. Finally, by combining the microstructure and composition analysis of C/SiC-ZrC composites, the ablation performance and mechanism of the materials were revealed.

3.1. Results

3.1.1. Macroscopic Morphology and Ablation Properties

Figure 3 shows the 2D needle-punched C/SiC-ZrC composites CSZ-40 and CSZ-20 after ablation. The macroscopic morphology of the two samples shows obvious erosion on the material surface, with distinct flow marks at the edges, and a circular pit in the middle, with a distributed white oxide layer [36,37]. The diameter of the pits in sample CSZ-20×2 is

slightly smaller than that in sample CSZ-40, and there are exposed black fibers and matrix in some areas. There are dotted white products outside the circular pit. In order to better observe the morphology inside the white oxide layer, the white oxide layer was removed. The morphology of the white oxide layer after removal is shown in Figure 4. It can be seen that the CSZ-40 sample has a flatter ablation surface than the CSZ-20×2 sample, with less fiber bundle breakage and damage. Compared to cyclic ablation, single ablation causes greater damage, a larger ablation amount, deeper ablation pits, and more exposed carbon fibers. Using an industrial scanner to reconstruct the macroscopic morphology of the sample after ablation, the front and side views of the three-dimensional macroscopic morphology are shown in Figure 5. Based on the three-dimensional macroscopic morphology, it can be seen that the maximum depth of cyclic ablation is 0.998 mm, which is lower than the maximum depth of single ablation of 1.293 mm. The depth distribution of cyclic ablation pits is more uniform, and the carbon fiber skeleton structure is almost invisible, indicating a lower linear ablation rate.

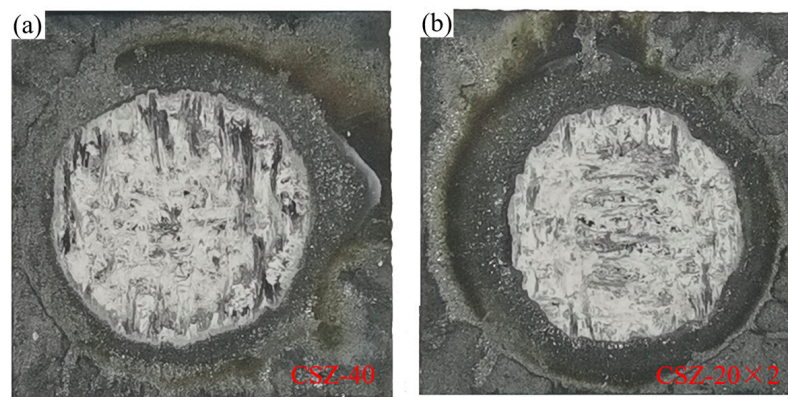


Figure 3. Comparison diagram of samples ablated with different ablation modes in 40 s. (a) Single ablation; (b) cyclic ablation.



Figure 4. Macroscopic morphology after removal of white oxide layer with different ablation modes in 40 s.

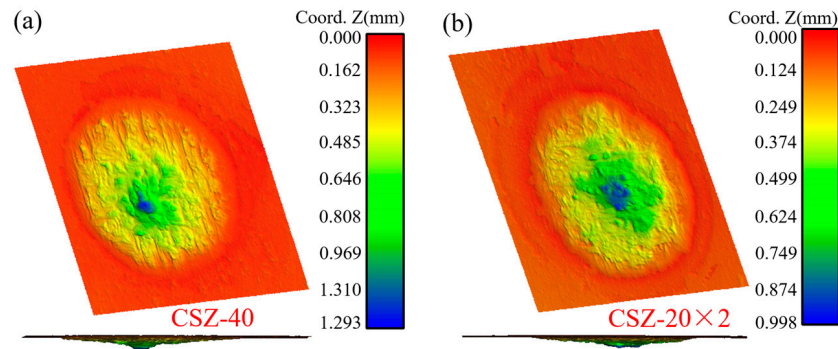


Figure 5. Three-dimensional morphology of ablation in 40 s. (a) Single ablation; (b) cyclic ablation.

Table 3 lists the line ablation rate and mass ablation rate of C/SiC-ZrC composites under different ablation modes. The line ablation rate and mass ablation rate of cyclic ablation are lower than those of single ablation at 30 s, 40 s, and 60 s. The average line ablation rate and mass ablation rate of cyclic ablation are 24.1 $\mu\text{m/s}$ and 6.9 mg/s , respectively. The average line ablation rate and mass ablation rate of single ablation are 27.4 $\mu\text{m/s}$ and 9.1 mg/s , respectively. Compared to single ablation, the average line ablation rate and mass ablation rate of cyclic ablation are reduced by 12% and 24.2%, respectively, with the mass ablation rate experiencing a greater reduction relative to the linear ablation rate. This indicates that the C/SiC-ZrC composites lose less mass under cyclic ablation, thus exhibiting better anti-ablation performance. The three-dimensional morphology reconstruction in Figure 5 also confirms that the cyclic ablation pits are shallower and more evenly distributed. Figure 6 shows the comparison between the line ablation rate and mass ablation rate. Due to the uneven surface of C/SiC composites and the uneven shape of the center region after ablation, different methods are used to measure the line ablation rate and the mass ablation rate. The line ablation rate is calculated by measuring the thickness of three positions before and after ablation and then taking the average value to calculate the line ablation rate with a tolerance band. The mass ablation rate is calculated by measuring the mass before and after ablation. Under the same ablation method, the line ablation rate and mass ablation rate peak at 30 s. Subsequently, both the line ablation rate and mass ablation rate gradually decrease with time. From 30 s to 60 s, the line ablation rate and mass ablation rate of C/SiC-ZrC under single ablation decreased by 14.1% and 26.2%, respectively. For cyclic ablation, the corresponding decreases were 15.6% and 16.4%, respectively. At any given ablation time, the line ablation rate and mass ablation rate of cyclic ablation are consistently lower than those of single ablation. The largest difference in the line ablation rate is observed at 40 s, reaching 15.7%, while the largest difference in the mass ablation rate is seen at 30 s, amounting to 31.8%.

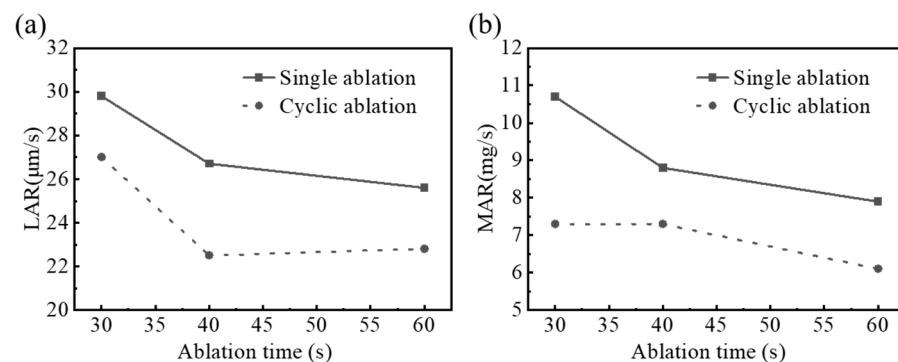


Figure 6. Comparison of ablation rates under single and cyclic ablation modes. (a) Linear ablation rate (LAR); (b) mass ablation rate (MAR).

Table 3. C/SiC-ZrC ablation rate results.

Materials	Parameters	CSZ-30	CSZ-15×2	CSZ-40	CSZ-20×2	CSZ-60	CSZ-30×2
C/SiC-ZrC	Ablation time/s	30	15 × 2	40	20 × 2	60	30 × 2
	Thickness before ablation/mm	5.168	5.170	5.158	5.197	5.156	5.161
	Thickness after ablation/mm	4.273	4.361	4.092	4.298	3.623	3.792
	LAR/($\mu\text{m}\cdot\text{s}^{-1}$)	29.8	27	26.7	22.5	25.6	22.8
	Mass before ablation/g	9.0482	8.9830	9.0260	9.1637	9.0794	9.1915
	Mass after ablation/g	8.7252	8.7637	8.6744	8.8723	8.6026	8.8254
	MAR/($\text{mg}\cdot\text{s}^{-1}$)	10.7	7.3	8.8	7.3	7.9	6.1

The cyclic ablation mode resulted in a more uniform depth distribution of the ablation pits and a flatter surface of the pits in the C/SiC-ZrC composites, compared to the single ablation mode. Its line ablation rate and mass ablation rate are significantly lower. This indicates that when C/SiC-ZrC composites are applied to cyclic high-temperature environments such as RDE, their ablation life cannot be calculated based on the ablation rate of the single ablation mode. Instead, the ablation rate of the cyclic ablation mode should be considered; thus, the actual service life of RDE will be higher than expected.

3.1.2. Microstructure and Morphology

The microstructures of samples CSZ-15×1 and CSZ-15×2 after ablation are shown in Figure 7. Three morphologies of C/SiC-ZrC composites can be observed following high-temperature ablation: the surface oxide layer, the carbon fiber wrapping layer, and carbon fiber damage. As depicted in Figure 7a, white products adhere to the surface of the material. Figure 7a Yellow boxed area enlarged as shown in Figure 7b, a white oxide layer is evident, formed by the oxidation of SiC and ZrC deposited on the surface of the composites. There are small gaps surrounding the white oxide layer, and spherical oxide particles can be observed in the gap area. The EDS analysis results for the A-B line in Figure 7b are presented in Figure 7g, revealing that the oxide particles consist of SiO₂ and a small amount of ZrO₂. SiO₂ is produced through the reaction of SiC with oxygen or water at high temperatures [38,39], while ZrC reacts with oxygen or water to produce ZrO₂ [40].

As shown in Figure 7c,d, the locally exposed fibers on the surface of the sample are wrapped by particles. Some carbon fibers break, and a large number of carbon fibers on the left side are ablated and damaged. Here, they are closer to the ablative center, experiencing the most severe ablative damage. The carbon fibers on the right side have a wrapping layer, and the matrix generates SiO₂ and ZrO₂ in a high-temperature oxidation environment, which slows down the ablation of carbon fibers within the C/SiC-ZrC composites [41]. The EDS analysis results of the C-D line in Figure 7d are shown in Figure 7h, where the carbon fiber cladding is composed of SiO₂ and a very small amount of ZrO₂. This indicates that the main component attached to the carbon fiber is SiO₂. Figure 7e,f show the damage morphology of carbon fibers perpendicular to the ablation direction. The carbon fibers on the material surface exhibit varying degrees of ablation damage, with a small amount of ZrO₂ and SiO₂ surrounding the carbon fibers. The carbon fibers become thinner, with a small amount of fiber fracture. The fiber surface is marked by ablation pits of varying sizes, suggesting that mechanical ablation occurs in the high heat flux ablation environment of the carbon fibers [42].

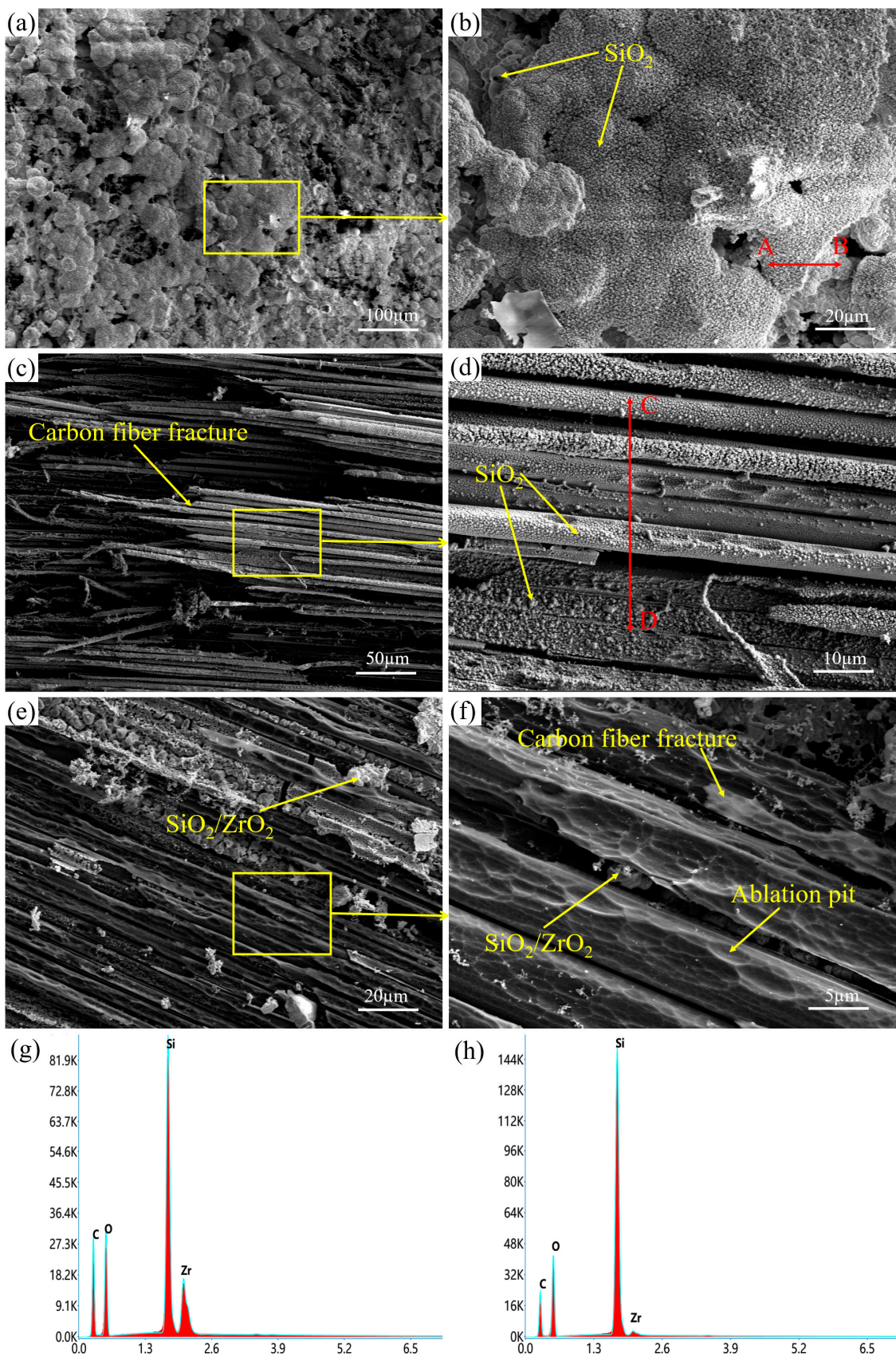


Figure 7. Micromorphology after ablation. (a,b) Matrix of CSZ-15×1; (c,d) carbon fiber oxide layer of CSZ-15×1; (e,f) carbon fiber ablation morphology of CSZ-15×2; (g) A-B line EDS spectroscopy analysis; (h) C-D line EDS spectroscopy analysis.

3.2. Analysis

From Figure 7c,d, it can be seen that there is a coating layer on the surface of the carbon fiber. According to the EDS composition analysis of the carbon fiber in Figure 7d, the coating layer of the carbon fiber is composed of SiO_2 and a small amount of ZrO_2 . The formation of SiO_2 and ZrO_2 can be attributed to the oxidation of the deposited matrix. The melting point of SiO_2 is $1723\text{ }^\circ\text{C}$, which is much lower than the melting point of ZrO_2 at $2700\text{ }^\circ\text{C}$. Under high-temperature conditions, SiO_2 first melts and penetrates deeper into the carbon fiber region, while ZrO_2 mostly remains on the surface and forms a eutectic structure with SiO_2 . During the ablation process, the material is removed by chemical ablation from oxygen, and mechanical ablation from high-speed airflow. The silicon carbide matrix first melts at high temperatures, and both the silicon carbide matrix and carbon fibers are oxidized. In areas with less severe heat flux ablation, the silicon carbide matrix oxidizes to form SiO_2 , which forms a dense and continuous oxide layer on the surface of the carbon fibers. SiO_2 contracts into a spherical shape during the cooling process [22]. At the bottom of Figure 7d, it can be seen that only half of the carbon fiber remains, and there are obvious ablation pits on the surface of the carbon fiber in the middle area. The surface is uniformly distributed, with an oxide layer and spherical oxide particles of different sizes, indicating that the carbon fiber, including the damaged carbon fiber, is uniformly wrapped by the oxide layer. This suggests that the SiC deposited on the surface of the composites forms an oxide layer distributed on the carbon fiber during the ablation process. Preventing heat and oxygen from coming into contact with carbon fibers slows down their ablation and improves their resistance to ablation and oxidation. After 30 days of ablation, the morphology of carbon fibers is shown in Figure 7e,f. The oxide coating of carbon fibers disappears, and various sizes of ablation pits are distributed on the surface of the carbon fibers. Some carbon fibers are severely damaged and have already fractured. A small amount of SiO_2 and ZrO_2 particles are scattered on the surface of the material, and there are many oxides distributed between the carbon fibers. This indicates that the oxide layer formed by a single ablation is melted and eroded again in the subsequent ablation process. The surface pits indicate severe mechanical ablation during the ablation process. During the melting and ablation of the oxide layer, heat is absorbed, and some of the heat is taken away when stripped, thus slowing down the process of secondary ablation.

As the ablation time increases, the ablation proceeds deeper into the material. The microstructure of sample CSZ-20 \times 1 is shown in Figure 8a,b, where some of the matrix is oxidized to form SiO_2 and ZrO_2 . White oxides can be seen on the ablated surface, but due to the ablation effect, a dense and continuous oxide layer cannot be formed. In the most severely eroded central area, some carbon fibers are exposed, which is caused by the matrix being eroded in a short time [43,44]. A small amount of SiO_2 and ZrO_2 particles are attached to the exposed carbon fibers. The microstructure of sample CSZ-30 is shown in Figure 8c, with needle-shaped cluster morphology [35,45]. The carbon fiber facing the ablation direction is the needle-punched structure of the composites. The proportion of various elements in the F region in Figure 8c is shown in Table 4, and it can be seen that the white oxide on the surface is composed of SiO_2 and ZrO_2 . From Figure 8c, it can be observed that the area with more SiO_2 and ZrO_2 exhibits less obvious carbon fiber ablation, and the morphology of the needle-shaped carbon fiber is uniform, with less ablation damage. The morphology of the carbon fiber head in the area with less SiO_2 and ZrO_2 is shown in Figure 8d. Du [35] found the same needle-like cluster morphology in the study of SiC/SiC composites, which appeared at the fiber breaks in the ablation center region. As shown in Figure 9a,b, the matrix near the SiC fibers in the central region of the ablation is burned out, resulting in the fibers being completely exposed to the ablation flame, whereas the matrix near the fibers in the text is ablated, but there is still a large number of oxide particles formed by ZrO_2 and SiO_2 adsorbed near the fibers. The distribution of SiO_2 and ZrO_2 can affect the ablation resistance of the carbon fiber. Due to the ablation of the material surface by high heat flux and high-speed airflow, the SiO_2 and ZrO_2 generated after oxidation are not uniformly distributed on the material surface. The area with less SiO_2 and ZrO_2 is

severely eroded. A uniformly distributed oxide layer can improve the ablation resistance of C/SiC-ZrC composites. The morphology of carbon fibers in the vertical ablation direction is shown in Figure 8e. The carbon fibers are severely eroded, and a small amount of SiO₂ and ZrO₂ particles are scattered on the surface of the fibers. There are large and small ablation pits on the surface of the carbon fibers. The carbon fibers near the surface have larger ablation pits and are finer, whereas the deeper carbon fibers have smaller ablation pits and are thicker. Some carbon fibers are broken, and the heads are pointed. There are more oxides distributed between the deeper carbon fibers. There are two typical ablation failure mechanisms in carbon fiber-reinforced ceramic composites: chemical ablation and mechanical exfoliation. Carbon fibers are oxidized in high-temperature environments, and the oxidation ablation is relatively uniform. Carbon fibers gradually become finer, and the ablation pits distributed on their surface indicate that they have been subjected to severe mechanical exfoliation. Based on the original defects and damage distribution of carbon fibers in Figure 8f [46], the formation of ablation pits is somewhat related to the initial damage of carbon fibers. The carbon fibers in the vertical ablation direction are completely exposed to a high-temperature environment, and they are gradually mechanically eroded and oxidized. Mechanical ablation first occurs at the initial damage position on the surface of the carbon fibers, resulting in the formation of small ablation pits on their surface. As ablation progresses, the ablation pits gradually increase in size. Combined with the scouring effect of high-speed airflow, carbon fibers break into large pits and fine areas. The ablative pits indicated by the arrow in Figure 8e are the points where the fibers are about to break, forming sharp spikes after fracture.

Table 4. EDS composition analysis.

Element	Weight (%)	Atomic (%)	Error (%)
O	52.3	78.2	10.3
Si	15.9	13.5	5.4
Zr	31.8	8.3	5.4

The microstructure of sample CSZ-15×1 is shown in Figure 10a,b, and it can be seen that the carbon fiber is mostly oxidized. The wrapping layer maintains a cylindrical shape, and there are fractures in the wrapping layer and local areas are burned. This is the same structure as that found by Du [47] for the surface layer of fibers after ablation. The carbon fiber that has been burned is only left at the center or completely disappears, and there are no other carbon fibers nearby. The carbon fiber wrapped in oxides deeper still maintains its intact morphology, while the carbon fiber without an oxide wrapping layer is severely burned. The carbon fiber wrapping layer significantly reduces the ablation rate of carbon fibers, mainly because the wrapping layer composed of SiO₂ and ZrO₂ can inhibit the inward diffusion of oxygen, protecting the internal carbon fibers. The dense oxide wrapping layer structure has a positive effect on the resistance of carbon fibers to ablation, thereby improving the ablation resistance of C/SiC-ZrC composites.

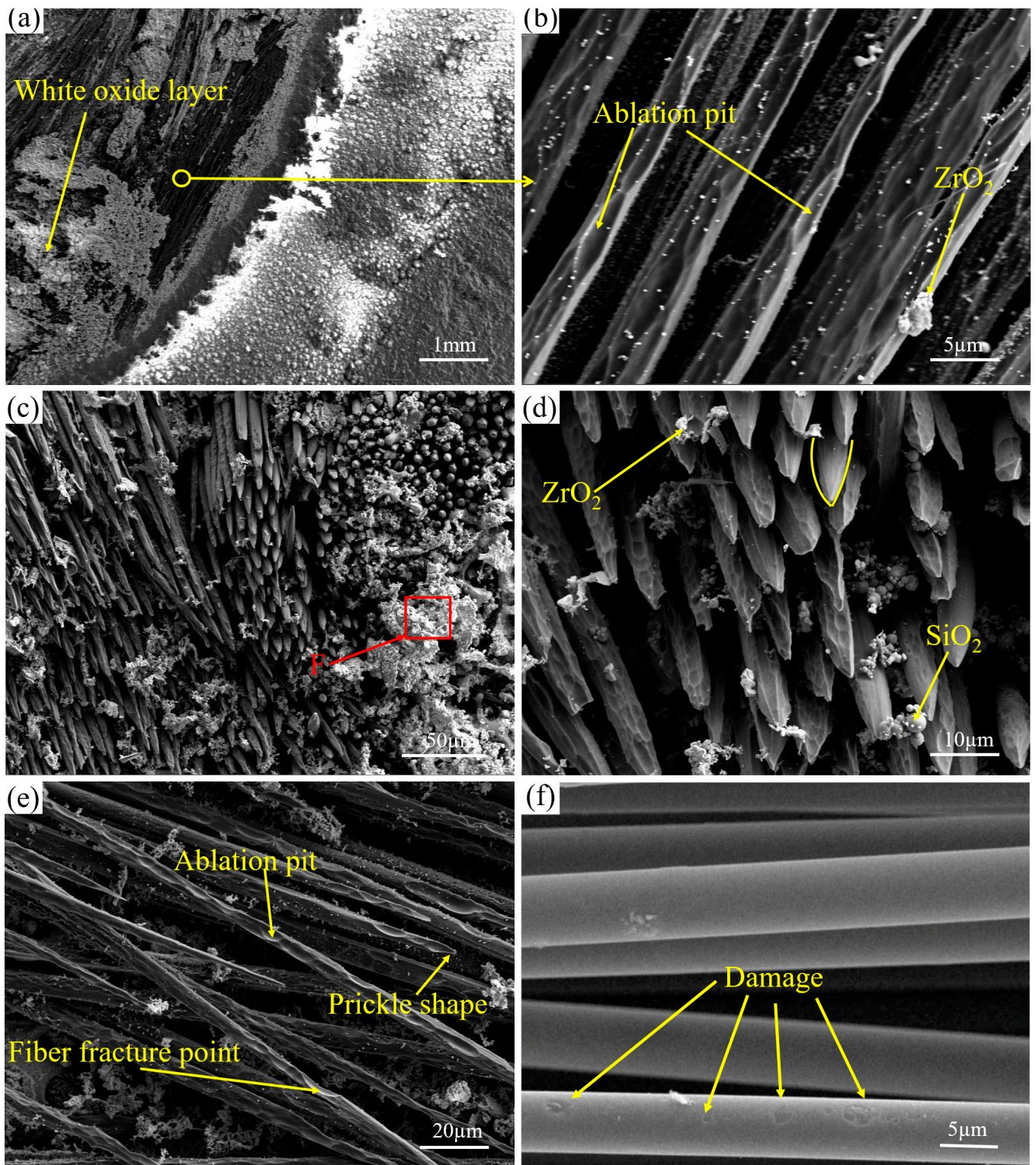


Figure 8. Morphology of carbon fibers on ablated surfaces. (a,b) Surface morphology of CSZ-20×1; (c–e) carbon fiber morphology of CSZ-30; (f) initial damage of carbon fibers [46].

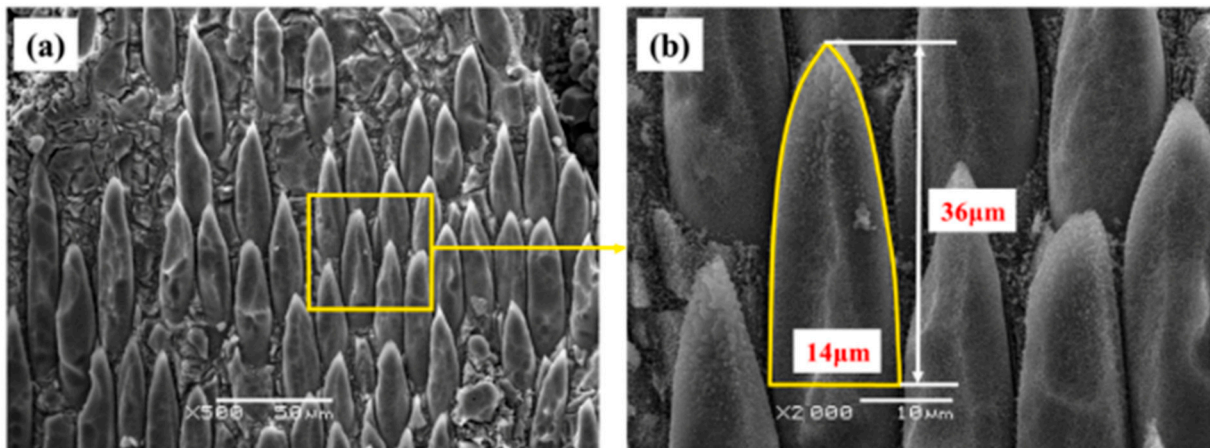


Figure 9. Ablation fracture morphology of fiber bundles [35]. (a) Needle-like tissue fracture morphology; (b) needle-like tissue size.

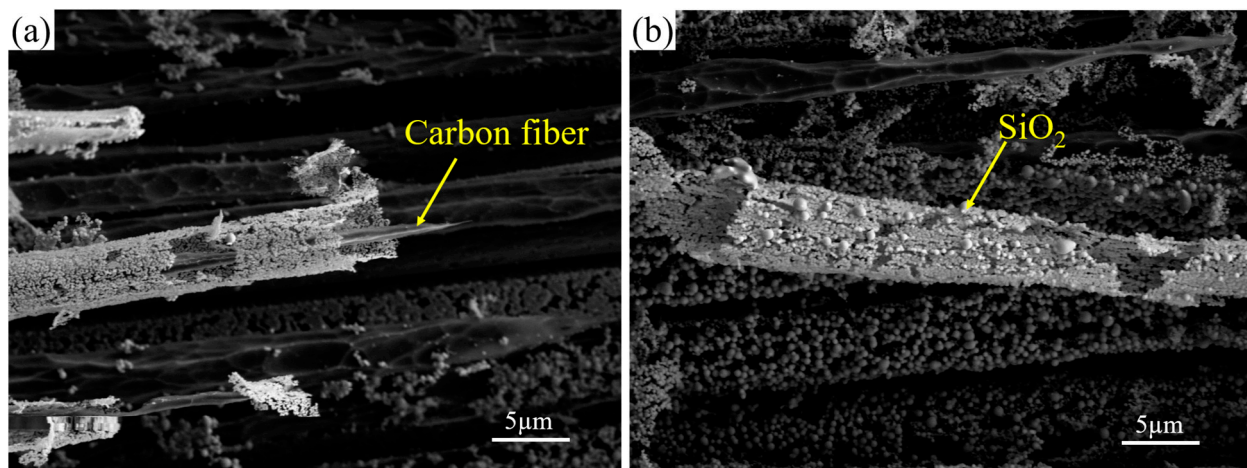


Figure 10. Morphology of the oxide layer on carbon fibers of CSZ-15×1. (a) Carbon fiber damage of CSZ-15×1; (b) carbon fiber oxide layer of CSZ-15×1.

4. Conclusions

The ablation test was conducted on C/SiC-ZrC composites using an oxyacetylene flame. The macroscopic and microscopic morphologies after ablation were observed, and the effects of different ablation modes on ablation parameters were compared. The ablation resistance mechanism of C/SiC-ZrC composites was analyzed, and the following conclusions were obtained:

(1) The average linear ablation rate and mass ablation rate for cyclic ablation are 12% and 24.2% lower than those for single ablation, respectively. The depth of ablation pits in cyclic ablation is shallower and more evenly distributed, indicating that the material exhibits better anti-ablation performance under the cyclic ablation mode. C/SiC-ZrC composites applied to RDE have a higher service life than expected.

(2) From 30 to 60 s, the linear ablation rate and mass ablation rate of single ablation decreased by 14.1% and 26.2%, respectively, while the linear ablation rate and mass ablation rate of cyclic ablation decreased by 15.6% and 16.4%, respectively.

(3) The C/SiC-ZrC composites form three main morphologies during the ablation process: a surface oxide layer, a carbon fiber wrapping layer, and carbon fiber damage.

(4) The reasons why C/SiC-ZrC composites have good ablation performance are as follows: firstly, the ZrC matrix resists the ablation of adjacent SiC matrices by heat flux, and the oxidized ZrO₂ also has the same effect on SiO₂. Secondly, the SiO₂ and ZrO₂ generated

by oxidation are distributed on the surface of the matrix and carbon fibers, inhibiting the diffusion of oxygen and slowing down the oxygen ablation of the matrix and carbon fibers.

Author Contributions: H.G.: conceptualization, methodology, modeling, investigation, formal analysis, writing—review and editing. L.Z.: investigation, modeling, analysis, data curation. H.Z. and F.W.: analysis, data curation. X.G. and Y.S.: investigation, funding acquisition. All authors have read and agreed to the published version of the manuscript.

Funding: This work was supported by the National Science and Technology Major Project (grant number: Y2019-I-0018-0017).

Data Availability Statement: The data sets generated during the current study are available from the corresponding author upon reasonable request.

Acknowledgments: We acknowledge the State Key Laboratory of Mechanics and Control for Aerospace Structures and the Key Laboratory of Aero-engine Thermal Environment and Structure, the Ministry of Industry and Information Technology, for providing research facilities for this work. The authors also wish to thank Du Jinkang and Zhang Sheng for their assistance in interpreting the significance of the results of this study.

Conflicts of Interest: The authors declare no conflict of interest.

References

- Anand, V.; Gutmark, E.J. Rotating Detonations and Spinning Detonations: Similarities and Differences. *AIAA J.* **2018**, *56*, 1717–1722. [[CrossRef](#)]
- Sam, L.; Idithsaj, P.T.; Nair, P.P.; Suryan, A.; Narayanan, V. Prospects for scramjet engines in reusable launch applications: A review. *Int. J. Hydrogen Energy* **2023**, *48*, 36094–36111. [[CrossRef](#)]
- Huang, W.; Du, Z.B.; Yan, L.; Moradi, R. Flame propagation and stabilization in dual-mode scramjet combustors: A survey. *Prog. Aerosp. Sci.* **2018**, *101*, 13–30. [[CrossRef](#)]
- Natali, M.; Kenny, J.M.; Torre, L. Science and technology of polymeric ablative materials for thermal protection systems and propulsion devices: A review. *Prog. Mater. Sci.* **2016**, *84*, 192–275. [[CrossRef](#)]
- Al-Jothery, H.K.M.; Albarody, T.M.B.; Yusoff, P.S.M.; Abdullah, M.A.; Hussein, A.R. A review of ultra-high temperature materials for thermal protection system. In *IOP Conference Series: Materials Science and Engineering, Proceedings of the Symposium on Energy Systems 2019 (SES 2019), Kuantan, Malaysia, 1–2 October 2019*; IOP Publishing: Bristol, UK, 2020; Volume 863, p. 012003.
- Uyanna, O.; Najafi, H. Thermal protection systems for space vehicles: A review on technology development, current challenges and future prospects—ScienceDirect. *Acta Astronaut.* **2020**, *176*, 341–356. [[CrossRef](#)]
- Fang, G.; Gao, X.; Song, Y. A review on ceramic matrix composites and environmental barrier coatings for aero-engine: Material development and failure analysis. *Coatings* **2023**, *13*, 357. [[CrossRef](#)]
- Lev, T.; Sanh, N.; Goon, S. Advanced sandwich structures for thermal protection systems in hypersonic vehicles: A review. *Compos. Part B Eng.* **2021**, *226*, 109301.
- Liu, L.; Li, H.; Shi, X.; Fu, Q.; Feng, W.; Yao, X.; Ni, C. Influence of SiC additive on the ablation behavior of C/C composites modified by ZrB₂–ZrC particles under oxyacetylene torch. *Ceram. Int.* **2014**, *40*, 541–549. [[CrossRef](#)]
- Chen, B.; Zhang, L.T.; Cheng, L.F.; Luan, X. Ablation Characteristic of 3D C/SiC Composite Nozzle in a Small Solid Rocket Motor. *J. Inorg. Mater.* **2008**, *23*, 938–944. [[CrossRef](#)]
- Sevastyanov, V.G.; Simonenko, E.P.; Gordeev, A.N.; Simonenko, N.P.; Kolesnikov, A.F.; Papynov, E.K.; Shichalin, O.O.; Avramenko, V.A.; Kuznetsov, N.T. HfB₂–SiC (45 vol %) ceramic material: Manufacture and behavior under long-term exposure to dissociated air jet flow. *Russ. J. Inorg. Chem.* **2014**, *59*, 1298–1311. [[CrossRef](#)]
- Shi, S.; Li, L.; Liang, J.; Tang, S. Surface and volumetric ablation behaviors of SiFRP composites at high heating rates for thermal protection applications. *Int. J. Heat Mass Transf.* **2016**, *102*, 1190–1198. [[CrossRef](#)]
- Wang, Y.; Risch, T.K.; Koo, J.H. Assessment of a one-dimensional finite element charring ablation material response model for phenolic-impregnated carbon ablator. *Aerosp. Sci. Technol.* **2019**, *91*, 301–309. [[CrossRef](#)]
- Natali, M.; Puri, I.; Rallini, M.; Kenny, J.; Torre, L. Ablation modeling of state of the art EPDM based elastomeric heat shielding materials for solid rocket motors. *Comput. Mater. Sci.* **2016**, *111*, 460–480. [[CrossRef](#)]
- Yu, G.; Du, J.; Zhao, X.; Xie, C.; Gao, X.; Song, Y.; Wang, F. Morphology and microstructure of SiC/SiC composites ablated by oxyacetylene torch at 1800 °C. *J. Eur. Ceram. Soc.* **2021**, *41*, 6894–6904. [[CrossRef](#)]
- Wang, S.; Li, H.; Ren, M.; Zuo, Y.; Yang, M.; Zhang, J.; Sun, J. Microstructure and ablation mechanism of C/C–ZrC–SiC composites in a plasma flame. *Ceram. Int.* **2017**, *43*, 10661–10667. [[CrossRef](#)]
- Li, J.; Yang, X.; Su, Z.A.; Xue, L.; Zhong, P.; Li, S.P.; Huang, Q.Z.; Liu, H.W. Effect of ZrC–SiC content on microstructure and ablation properties of C/C composites. *Trans. Nonferrous Met. Soc. China* **2016**, *26*, 2653–2664. [[CrossRef](#)]
- Tian, W.; Bai, X.; Guo, C.Y. Oxidation ablation resistance mechanism of C/C–SiC–HfB₂ composite. *J. Solid Rocket. Technol.* **2019**, *42*, 724–729.

19. Liu, R.; Liu, X.; Wang, Y.; Miao, H.; Song, C.; Qi, G.; Wan, F. Laser ablation behavior and mechanism of Cf/SiC-ZrC ultra-high temperature ceramic matrix composite prepared by PIP method. *Ceram. Int.* **2021**, *47*, 23610–23619. [[CrossRef](#)]
20. Xiang, Y.; Li, W.; Wang, S.; Chen, Z.H. Oxidation behavior of oxidation protective coatings for PIP-C/SiC composites at 1500 °C. *Ceram. Int.* **2012**, *38*, 9–13. [[CrossRef](#)]
21. Zhao, Z.G.; Li, K.Z.; Li, W. Ablation behavior of ZrC-SiC-ZrB₂ and ZrC-SiC inhibited carbon/carbon composites components under ultrahigh temperature conditions. *Corros. Sci.* **2021**, *189*, 109598. [[CrossRef](#)]
22. Fan, X.; Dang, X.; Ma, Y.; Yin, X.; Zhang, L.; Cheng, L. Microstructure, mechanical and ablation behaviour of C/SiC-Si with different preforms. *Ceram. Int.* **2019**, *45*, 23104–23110. [[CrossRef](#)]
23. Zhao, Z.; Li, K.; Li, W.; Zhang, L. Cyclic ablation behavior of C/C-ZrC-SiC-ZrB₂ composites under oxyacetylene torch with two heat fluxes at the temperatures above 2000 °C. *Corros. Sci.* **2021**, *181*, 109202. [[CrossRef](#)]
24. Chen, Z.; Fang, D.; Miao, Y.; Yan, B. Comparison of morphology and microstructure of ablation centre of C/SiC composites by oxy-acetylene torch at 2900 and 3550 °C. *Corros. Sci.* **2008**, *50*, 3378–3381. [[CrossRef](#)]
25. Song, C.; Ye, F.; Cheng, L. Long-term ceramic matrix composite for aeroengine. *J. Adv. Ceram.* **2022**, *11*, 1343–1374. [[CrossRef](#)]
26. Wang, Y.; Chen, Z.; Yu, S. Ablation behavior and mechanism analysis of C/SiC composites. *J. Mater. Res. Technol.* **2016**, *5*, 170–182. [[CrossRef](#)]
27. Raman, V.; Prakash, S.; Gamba, M. Nonidealities in rotating detonation engines. *Annu. Rev. Fluid Mech.* **2023**, *55*, 639–674. [[CrossRef](#)]
28. Wang, G.; Liu, S.; Peng, H.; Liu, W. Experimental Investigation of a Cylindrical Air-Breathing Continuous Rotating Detonation Engine with Different Nozzle Throat Diameters. *Aerospace* **2022**, *9*, 267. [[CrossRef](#)]
29. Shi, L.; Fan, E.; Shen, H.; Wen, C.Y.; Shang, S.; Hu, H. Numerical study of the effects of injection conditions on rotating detonation engine propulsive performance. *Aerospace* **2023**, *10*, 879. [[CrossRef](#)]
30. Ge, H.; Zhang, L.; Feng, F.; Du, J.; Huan, T.; Gao, X.; Song, Y. Comparative Ablation Behaviors of 2D Needled C/SiC and C/SiC-ZrC Composites. *Coatings* **2024**, *14*, 480. [[CrossRef](#)]
31. TORAY® Fiber Product Data [EB/OL]. Available online: https://www.torayca.cn/lineup/product/pro_001_01.html (accessed on 4 May 2020).
32. Zhang, S.; Gao, X.G.; Song, Y.D. In situ strength model for continuous fibers and multi-scale modeling the fracture of C/SiC composites. *Appl. Compos. Mater.* **2019**, *26*, 357–370. [[CrossRef](#)]
33. Mei, H.; Cheng, L.F. Comparison of the mechanical hysteresis of carbon/ceramic matrix composites with different fiber preforms. *Carbon* **2009**, *47*, 1034–1042. [[CrossRef](#)]
34. GJB232A-96; Test Methods for Ablation of Ablators. Military Standard Publishing House of the National Defense Science and Technology Commission: Beijing, China, 1997.
35. Du, J.; Yu, G.; Jia, Y.; Ni, Z.; Gao, X.; Song, Y.; Wang, F. Ultra-high temperature ablation behaviour of 2.5 D SiC/SiC under an oxy-acetylene torch. *Corros. Sci.* **2022**, *201*, 110263. [[CrossRef](#)]
36. Feng, B.; Li, H.; Zhang, Y.; Liu, L.; Yan, M. Effect of SiC/ZrC ratio on the mechanical and ablation properties of C/C-SiC-ZrC composites. *Corros. Sci.* **2014**, *82*, 27–35. [[CrossRef](#)]
37. Yan, C.; Liu, R.; Cao, Y.; Zhang, C.; Zhang, D. Ablation behavior and mechanism of C/ZrC, C/ZrC-SiC and C/SiC composites fabricated by polymer infiltration and pyrolysis process. *Corros. Sci.* **2014**, *86*, 131–141. [[CrossRef](#)]
38. Cui, Y.; Li, A.; Li, B.; Ma, X.; Bai, R.; Zhang, W.; Ren, M.; Sun, J. Microstructure and ablation mechanism of C/C-SiC composites. *J. Eur. Ceram. Soc.* **2014**, *34*, 171–177. [[CrossRef](#)]
39. Weng, Y.; Yang, X.; Chen, F.; Zhang, X.; Shi, A.; Yan, J.; Huang, Q. Effect of CVI SiC content on ablation and mechanism of C/C-SiC-ZrC-Cu composites. *Ceram. Int.* **2022**, *48*, 7937–7950. [[CrossRef](#)]
40. Zhao, Z.; Li, K.; Kou, G.; Li, W. Comparative research on cyclic ablation behavior of C/C-ZrC-SiC and C/C-ZrC composites at temperatures above 2000 °C. *Corros. Sci.* **2022**, *206*, 110496. [[CrossRef](#)]
41. Balat, M.J.H. Determination of the active-to-passive transition in the oxidation of silicon carbide in standard and microwave-excited air. *J. Eur. Ceram. Soc.* **1996**, *16*, 55–62. [[CrossRef](#)]
42. Li, H.J.; Yao, X.Y.; Zhang, Y.L.; Li, K.Z.; Guo, L.J.; Liu, L. Effect of heat flux on ablation behaviour and mechanism of C/C-ZrB₂-SiC composite under oxyacetylene torch flame. *Corros. Sci.* **2013**, *74*, 265–270. [[CrossRef](#)]
43. Fan, X.; Yin, X.; Wang, L.; Cheng, L.; Zhang, L. Processing, microstructure and ablation behavior of C/SiC-Ti₃SiC₂ composites fabricated by liquid silicon infiltration. *Corros. Sci.* **2013**, *74*, 98–105. [[CrossRef](#)]
44. Fang, D.; Chen, Z.; Song, Y.; Sun, Z. Morphology and microstructure of 2.5 dimension C/SiC composites ablated by oxyacetylene torch. *Ceram. Int.* **2009**, *35*, 1249–1253. [[CrossRef](#)]
45. Lachaud, J.; Aspa, Y.; Vignoles, G.L. Analytical modeling of the steady state ablation of a 3D C/C composite. *Int. J. Heat Mass Transf.* **2008**, *51*, 2614–2627. [[CrossRef](#)]
46. Zhang, S. Multi-Scale Analysis of the Mechanical Behavior for Braided Ceramic Matrix Composites. Ph.D. Thesis, Nanjing University of Aeronautics and Astronautics, Nanjing, China, 2020.
47. Du, J.; Yu, G.; Zhang, H.; Jia, Y.; Chen, R.; Liu, C.; Gao, X.; Wang, F.; Song, Y. Microstructural evolution mechanism of plain-woven SiC/SiC during thermal ablation. *Corros. Sci.* **2022**, *208*, 110679. [[CrossRef](#)]

Disclaimer/Publisher's Note: The statements, opinions and data contained in all publications are solely those of the individual author(s) and contributor(s) and not of MDPI and/or the editor(s). MDPI and/or the editor(s) disclaim responsibility for any injury to people or property resulting from any ideas, methods, instructions or products referred to in the content.